Journal of Materials Science Research and Reviews

Volume 7, Issue 4, Page 663-675, 2024; Article no.JMSRR.124216

Microstructure and Mechanical Properties of Fully Annealed Compacted Graphite Cast Iron for Automotive Applications

Adeniyi Ayodele Samuel [a*], Seidu Saliu [a++] and Oyetunji Akinlabi [a++]

[a] *Department of Metallurgical and Materials Engineering, Federal University of Technology, Akure, Nigeria.*

Authors' contributions

This work was carried out in collaboration among all authors. All authors read and approved the final manuscript.

Article Information

Open Peer Review History:
This journal follows the Advanced Open Peer Review policy. Identity of the Reviewers, Editor(s) and additional Reviewers, peer review comments, different versions of the manuscript, comments of the editors, etc are available here: https://www.sdiarticle5.com/review-history/124216

Original Research Article

Received: 29/07/2024
Accepted: 03/10/2024
Published: 14/10/2024

ABSTRACT

The work was conducted to determine the mechanical properties of heat-treated (full annealing) compacted graphite cast irons (CGI) of different microstructures suitable for automotive applications. Six types of CGI were selected from numerous available samples based on their chemical compositions. The six CGI were tagged A1, A2, A3, A4, A5, and A6. Full annealing heat-treated was carried out on A1-A6, they were austenized at 920°C. Chemical analysis and carbon equivalent were done, and the results showed that A1-A6 were hypereutectic CGI with different alloying elements. SEM analysis was equally carried out on A1 to A6. The result from the

[++] *Professor;*
**Corresponding author: Email: ayodeleadeniyi128@yahoo.com;*

Cite as: *Samuel, Adeniyi Ayodele, Seidu Saliu, and Oyetunji Akinlabi. 2024. "Microstructure and Mechanical Properties of Fully Annealed Compacted Graphite Cast Iron for Automotive Applications". Journal of Materials Science Research and Reviews 7 (4):663-75. https://journaljmsrr.com/index.php/JMSRR/article/view/358.*

microstructural analysis indicated that A1 and A2 have structures close to gray cast iron, A3 and A4 have a pure CGI microstructure, and A5 and A6 have structures close to ductile cast iron. Mechanical properties (hardness, impact, and wear resistance) were tested on A1-A6. A1 with 209 Brinell hardness number (HBN) has the highest hardness value and A6 with 112HBN has the least hardness number. Similarly, the result from ultimate tensile strength (UTS) shows that A5 has the highest UTS value of 140 megapascal (MPa) and A2 has the lowest value of 38MPa. 38.8J for A1 is the highest impact energy recorded for the series. Lastly, 67% recorded for A6 was the highest wear loss for the series. A1-A6 is suitable for the production of automotive parts especially exhaust system parts and engine blocks.

Keywords: Full annealing; mechanical property; compacted graphite cast irons; microstructures; automotive.

1. INTRODUCTION

Cast iron is an alloy of iron and carbon with carbon content generally between 2% and 4.5 [1]. It contains silicon which is an important ingredient, manganese, phosphorus, and sulfur [2]. Cast iron differs widely in composition and properties. Normal grades of cast iron are not particularly strong and are quite brittle [3]. A new brand of cast iron that will mitigate the disadvantages of normal cast iron is the compacted graphite cast iron (CGI). It has a carbon content between 3.1 and 4.0 % and silicon content of 1.7 and 3.0% [4].

This type of cast iron has graphite particles shaped like a cross between ductile iron, which has graphite in a sphere, and regular gray iron flakes [5]. The physical characteristics of the worm-like compacted graphite shape are similar to the best qualities of ductile and grey irons [6].

Since the 1940s, compacted graphite iron (CGI), also known as vermicular graphite iron, has been the most recent addition to the cast iron family [7]. Because vermicular, or worm-shaped, graphite is typically stubby and has blunt edges, CGI has a nice mix of mechanical and physical qualities that lie between ductile and gray cast iron [8]. Compacted graphite cast iron also has excellent tensile strength, good fracture toughness, and solid impact properties [9]. In addition, it has a high thermal conductivity and better resistance to thermal shock in engineering firms [10]. Compared to ductile cast iron, CGI has greater thermal conductivity, easier casting, and greater strength and stiffness) [11]. Because of its distinct resistance to thermal fatigue, it is very appropriate for use in internal combustion engines and braking components, among other uses [12].

When compared to metals like steel and gray cast iron, CGI is lighter and less expensive [13]. The car industry's growing need for cast lightweight materials like aluminum and metal-matrix composites has fueled the development of novel or more effective manufacturing processes and procedures [14]. Cast iron's low cost of manufacture has kept it competitive even with all the energy used in creating those new lightweight alloys [15].

Most of the mechanical properties of cast irons and their alloys depend on their microstructure [16]. They can be changed by varying the microconstituents in the metal through a heat-treatment process [17]. Full annealing of compacted graphite cast irons (CGI) is a heat treatment process designed to refine the microstructure, reduce hardness, increase ductility, and improve machinability [18]. It involves utilizing a hypereutectic CGI slowly to a temperature of 920° C and cooling in the furnace to produce ferritic microstructures [19].

Compacted graphite cast irons (CGI) are known for their excellent combination of strength, thermal conductivity, and resistance to thermal fatigue, making them suitable for a variety of demanding applications [20]. In the automobile industry, its higher strength and stiffness compared to gray cast iron, with better thermal conductivity and fatigue resistance than ductile iron makes it an excellent material for the production of engine blocks. cylinder heads, exhaust system parts [21]. It also finds a variety of applications in the production of wind turbines, and turbine housing, and in industries like marine, railroads, agricultural equipment, heavy machinery, and construction equipment [22].

2. EXPERIMENTAL PROCEDURES

Six compacted graphite cast iron of 16mm by 16crm in dimension were taken to the laboratory to determine their chemical compositions and

heat-treated in the furnace. After, the heat-treated process, mechanical tests were carried out on the six samples terms A1, A2, A3, A4, A5, and A6.

2.1 Determination of the Composition Analysis of CGI

Skyray EDX 3600B energy dispersive X-ray fluorescence spectrometer was used to determine the elemental composition of six different CGI before full annealing was carried out in the furnace. X-ray fluorescence is a powerful technique used in a wide variety of elemental composition of various materials [23]. XRF analyzers are widely recognized as a means for accurate, rapid, and non-destructive testing [24]. The Skyray EDX3600B is a high-end energy dispersive spectrometer with a large sample chamber that supports most sample size [25].

2.2 Full Annealing Heat Treatment

Full annealing was done on samples A1 to A6 using a muffle furnace. This compacted graphite cast iron produced was austenized at 920 °, held for 45 minutes, and cooled slowly in the furnace. The ductile resulting austenized materials made from this process are labeled A1, A2, A3, A4, A5, and A6.

2.3 Carbon equivalent of the Heat-Treated CGI

The carbon equivalent of the CGI was calculated using Equation 1 [26]

$$CE = C + (Mn + Si)/6 + (Cu + Ni)/15 + (V + Mo + Cr)/5 \quad (1)$$

Where CE is carbon equivalent, C is % by weight of carbon, Mn is % by weight of manganese, Si is the % by weight of silicon, Cu is the % by weight of copper, Ni is the % by weight of a nickel, V is the % by weight of vanadium, Mo is the % by weight of molybdenum, Cr is the % by weight of chromium that is present in CGI.

2.4 Microstructural Examination

2.4.1 SEM analysis

The scan electron microscopy (SEM) was carried out using a Carl Zeiss sigma field Emission gun scanning electron microscope under 1000 magnification of 10µm, with an energy dispersive spectrometer (EDS Scanning electron) these was done to examine the internal structures of the CGI produced to determine their degree of graphite growth and nodularity [27].

2.4.2 Hardness test

The hardness test was conducted using the hand-held Brinell tester. This conforms to ISO and ASTM E03-18 [28] standard which was used on all metals and alloys on any sample size [29]. The set of tests was performed on A1-A6, the test was done on four occasions and the average was recorded.

2.4.3 Tensile tests

Tensile tests were performed on the six samples of CGI produced labeled A1-A6 using the universal testing machine. The UTS test was carried out by ASTM A842-11A (2022) standard. The material testing system with a load capacity of 50 kN, at a loading speed of 10 rpm and a maximum chuck diameter of 1 0mm. The test samples were prepared on the lathe machine in cylindrical shapes of 9mm x 16cm. The samples were inserted into the chuck and were closely by an aligned key to grip them and the samples were pulled apart until they broke into pieces.

2.4.4 Impact strength

Impact strength was evaluated on the heat-treated samples labeled A1, A2, A3, A4, A5, and A6. The test was conducted using the ASTM standard of dimension 9 mm x 16mm using the Hounsfield balance impact machine. The V-notch impact specimen was clamped into the pendulum chuck and locked with an align key, the notched side facing the striking edge direction. The pendulum was released at a velocity of 4 m/s with a maximum energy of 170 these were done to fracture the materials and the energy absorbed by the materials was noted and recorded. Four tests were carried out on each specimen and their average was recorded in joules which are units of energy [30].

2.4.5 Wear test

The wear test of samples was carried out according to ASTM G99.15. The step-on disc rolling dry wear method was used which was carried out using a Rolling Sliding wear tester.

The initial mass M1 of samples was recorded before allowing them to be in contact with a rolling disc for one minute at 20 cycles. The final mass M2 of the samples was also recorded. The wear index R was obtained by Equation (2) [31].

$$R = \frac{M1 - M2}{RPM} \times 100\% \quad (2)$$

Where M_1 is the initial mass (g), M_2 is the final mass (g), and RPM =20.

3. RESULTS AND DISCUSSION

3.1 Elemental analysis of the Heat-Treated CGI (A1-A6)

Based on the theoretical failure analysis and chemical compositions of some selected silencers, the following CGI were obtained with varying alloying elements, tagged A1, A2, A3, A4, A5, and A6. Results from chemical composition analysis in Table 1, shown that CGIs obtained were hypereutectic irons with 4.35% carbon with the presence of Cu, and Cr which aids the increase of the pearlite phase so as to increase the hardness, heat resistance and strength which is in agreement with (32). These is shown in A1 and A2. Al. Ni and Si found in A4 and A5 were obtained purposely so as to aid graphitization which promote ferritic phase and aid ductility in accordance with Boulifa and Hadji [32]. Inaddition, Ni and Cr also increase thermal conductivity but it shown a deleterious effect on percentage elongation, UTS and toughness as seen in A3 and A6 according to [33].

3.2 Carbon equivalent of the Heat-Treated CGI Materials (A1-A6)

The carbon equivalent (CE) of the CGI is shown in Table 2. All the CGI from A1-A6 are in excellent condition and fall into the range of CE of CGI which should be greater than 4.35 which is in line with [34].

3.3 SEM Analysis of A1-A6

Fig. 1 shown a CGI with a distorted clusters graphite flakes (DGF) in ferrite under 1000 magnification. The microstructure of A1 is close to gray cast iron with little percentage of nodules in the ferrite phase.

Fig. 2 shows several distorted graphite flakes (DGF) in ferrite under 1000 magnification. The microstructure of A2 is also close to gray cast iron with a small percentage of distorted nodules (DN) in the ferrite phase. The nodules in A2 are more than the ones in A1.

Fig. 3 shows several distorted graphite flakes (DGF) in ferrite under 1000 magnification. Some of the distorted graphite flakes are separated. The microstructure of A3 is pure compacted graphite cast iron with an equal number of distorted nodules (DN) in the ferrite phase.

Fig. 4. shows several distorted graphite flakes (DGF) in ferrite under 1000 magnification. Some of the distorted graphite flakes are separated. The microstructure of A4 is also a pure compacted graphite cast iron with an equal number of distorted nodules (DN) in the ferrite phase. The nodules in A4 are smaller in size than the nodules in A3 because of the percentage of Cu which served as nodules reducer (anti-nodularizers) in accordance with [35].

Fig. 5 shows several heavily distorted graphite flakes (DGF) in ferrite under 1000 magnification. Some of the distorted graphite flakes are separated. The microstructure of A5 is more ductile cast iron with some distorted nodules (DN) in the ferrite phase. The nodules in A5 are bigger in size than the nodules in A1 to A4 because of the percentage of silicon, magnesium which served as nodule enhancers which agrees with [4].

Table 1. Summary Elemental Composition of the Heat-Treated CGI Materials (A1-A6)

	Fe	C	Si	Cu	Cr	Ti	AL	Ni	Mg	S	Mn
A1	93.1000	4.3500	1.5400	0.1510	0.0773	0.0067	0.2090	0.0466	0.0025	0.0953	0.216
A2	92.6000	4.3500	1.8200	0.1820	0.0900	0.0134	0.1610	0.0438	0.0064	0.1390	0.2800
A3	92.5000	4.3500	1.8800	0.1820	0.0943	0.0211	0.1620	0.0433	0.0038	0.1350	0.2590
A4	92.4000	4.3500	2.0000	0.3150	0.1310	0.0183	0.0307	0.0531	0.0048	0.1320	0.2770
A5	92.0000	4.3500	2.2300	0.3290	0.1450	0.017	0.0597	0.1790	0.0081	0.1440	0.2820
A6	92.4000	4.3500	2.0200	0.3400	0.1200	0.0374	0.0294	0.0053	0.0053	0.1200	0.2760

Table 2. Carbon equivalent of the Heat-Treated CGI Materials (A1-A6)

SN	C1	C2	C3	C4	C5	C6
CE	4.65	4.85	4.96	4.78	4.83	4.79

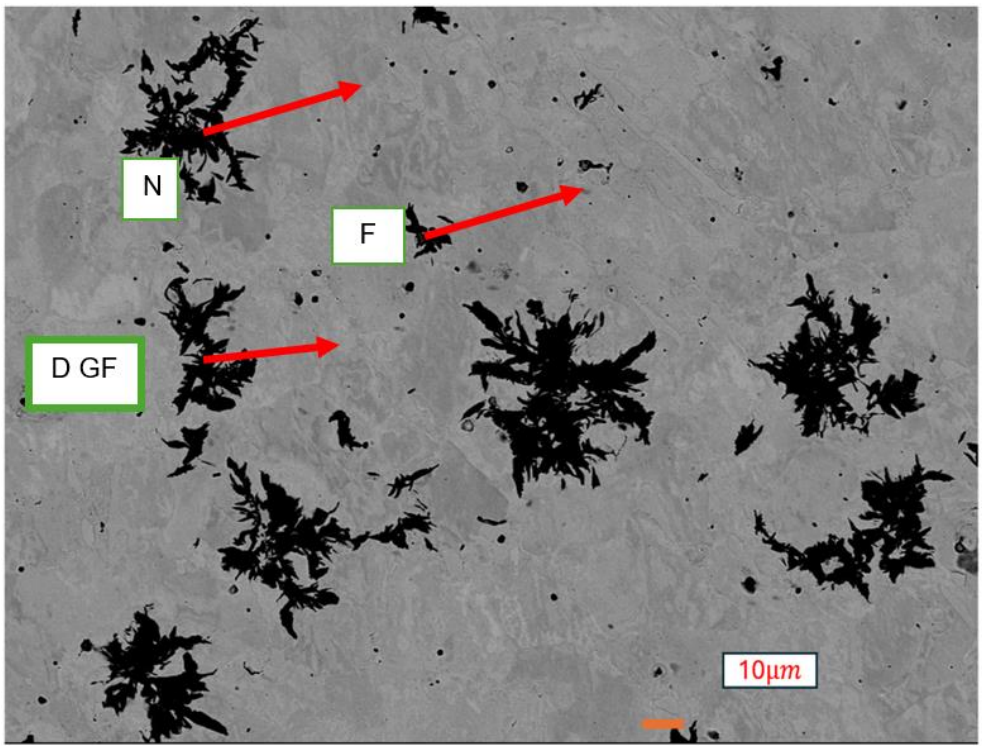

Fig. 1. A1 SEM image
DGF= Distorted graphite flakes in ferrite, F= ferrite, N= nodules

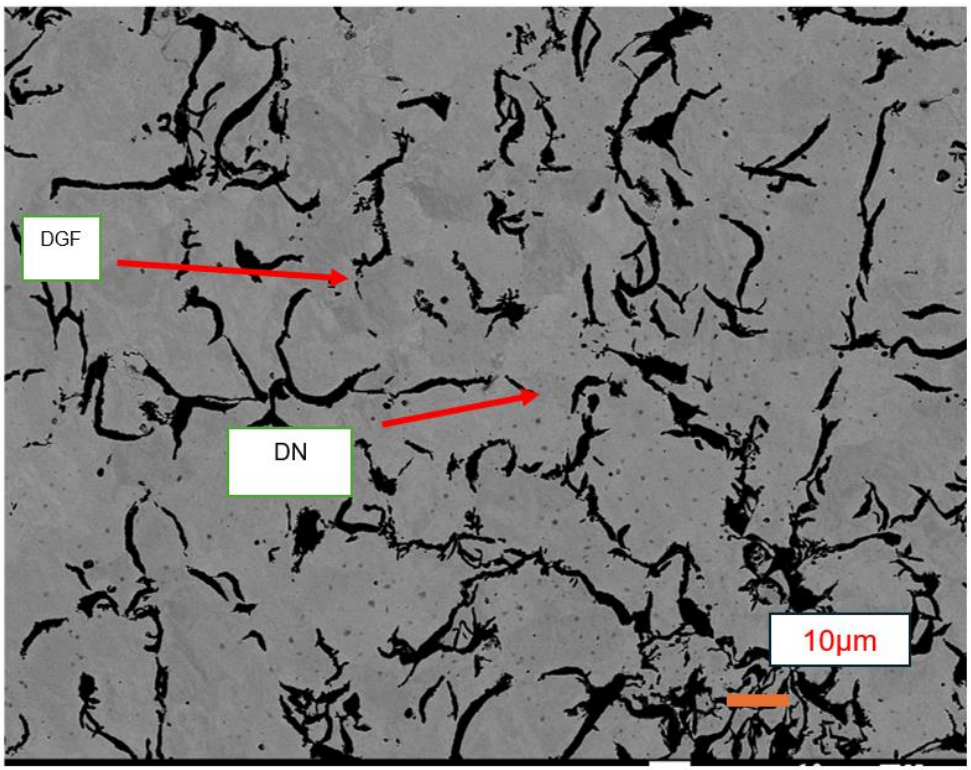

Fig. 2. A2 SEM image
DGF= Distorted graphite flakes in ferrite, F= ferrite, DN= distorted nodules

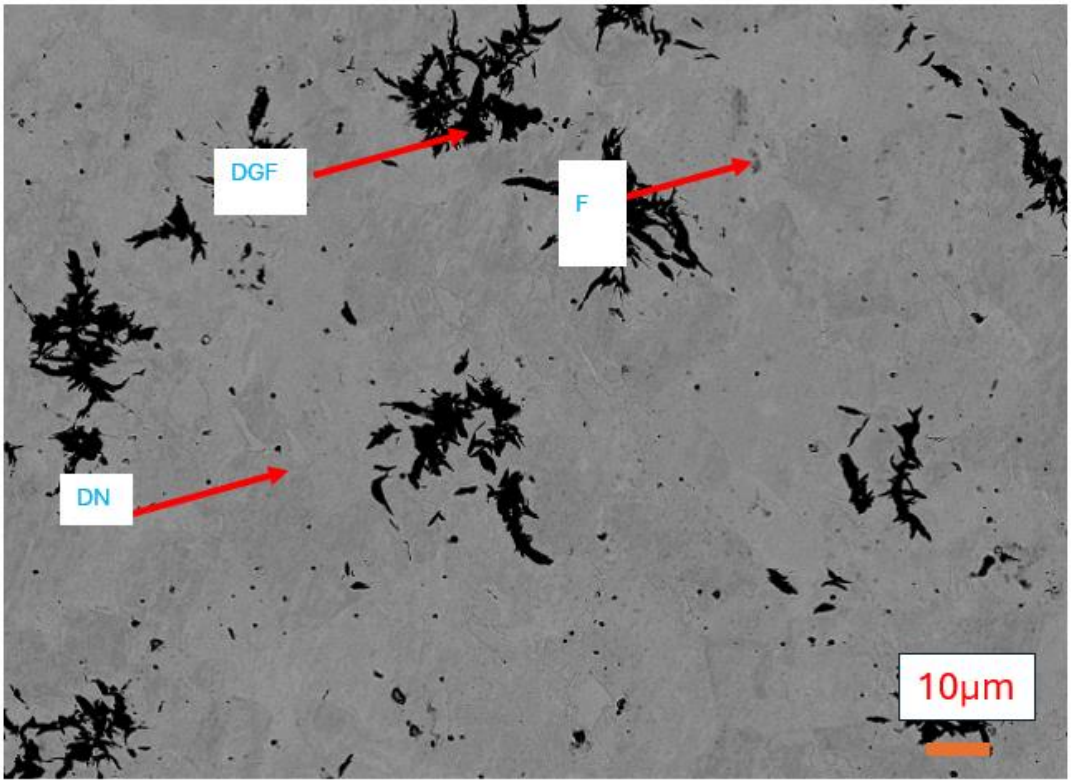

Fig. 3. A3 SEM image
DGF= Distorted graphite flakes in ferrite, F= ferrite, DN= distorted nodules

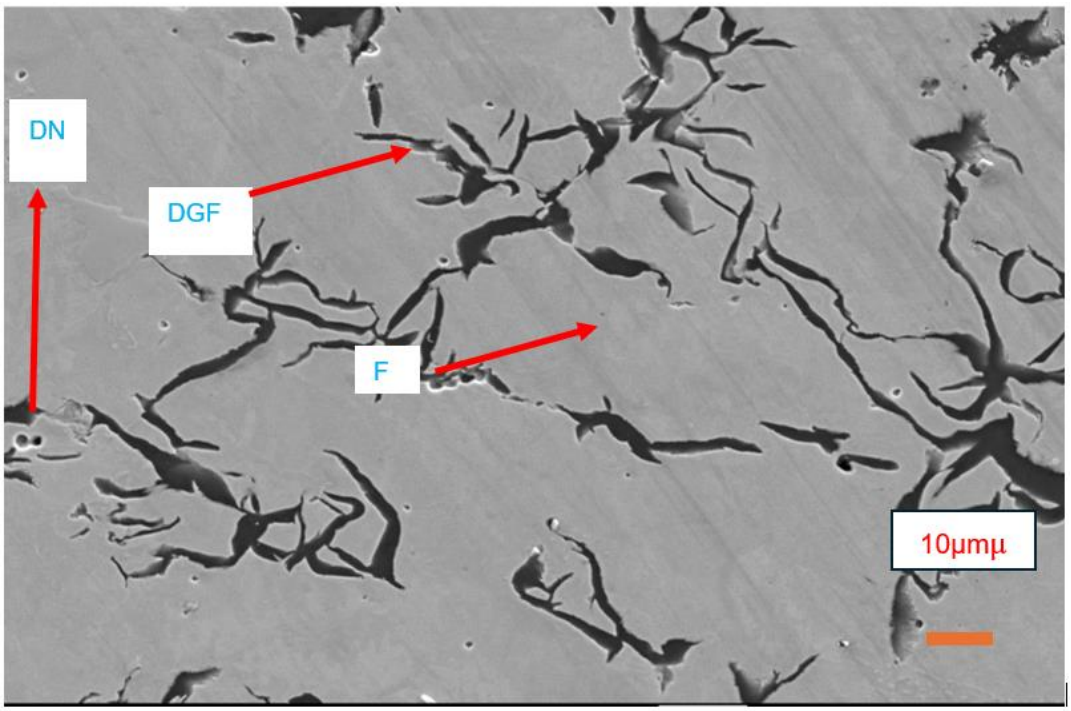

Fig. 4. A4 SEM image
DGF= Distorted graphite flakes in ferrite, F= ferrite, DN= distorted nodules

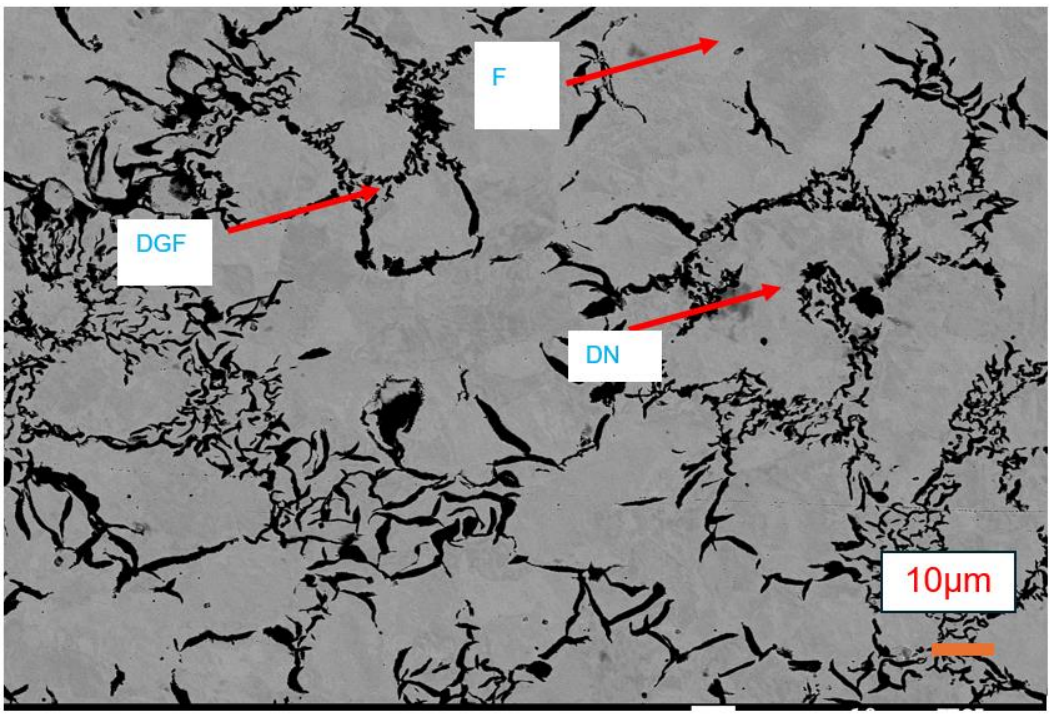

Fig. 5. A5 SEM image
DGF= Distorted graphite flakes in ferrite, F= ferrite, DN= distorted nodules

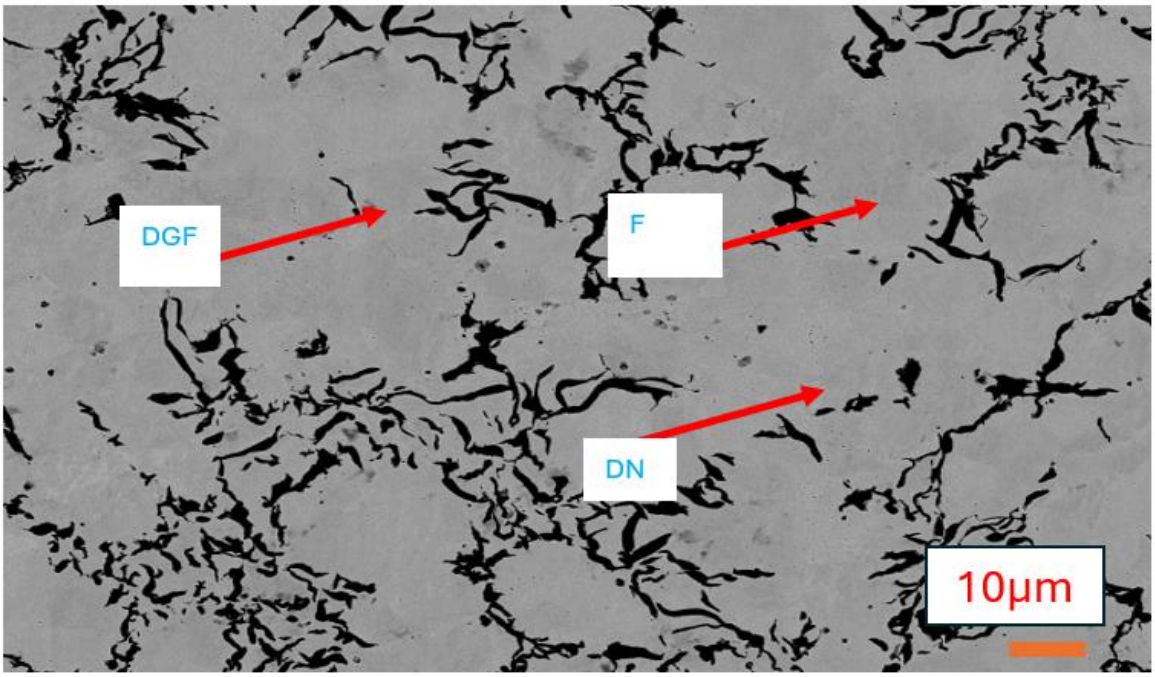

Fig. 6. A6 SEM image
DGF= Distorted graphite flakes in ferrite, F= ferrite, DN= distorted nodules

Fig. 6 shows several heavily distorted graphite flakes (DGF) in ferrite under 1000 magnification. Some of the distorted graphite flakes are separated. The microstructure of A6 is more ductile cast iron with some distorted nodules (DN) in the ferrite phase. The nodules in A6 are also bigger than the nodules in A1 to A4 because of the percentage of silicon which

served as a nodules enhancer and copper which increased the pearlitic phase. which agrees with [36].

3.3.1 Hardness

The hardness results of A1 to A6 from Fig. 7 reveal, that the materials are tough, ductile, and have some elements of plastic deformation before failure. These conditions are desirable as they give a warning before failures in accordance with [37]. Also, A1 has the highest Brinel hardness (HB) value of 209 because its structure is close to gray iron microstructure, followed by sample A4 with 183HB this is due to the high percentage of Cu, Cr, and Mn which increase the hardness of CGI in accordance with [38]. The lowest is sample A6 with 112HB values because it's ductile cast iron and ductile cast iron has the least hardness value in comparison to gray and compacted graphite cast iron which is in line with [39]. Summarily, all the samples' microstructures are mostly ferritic with a little blend of pearlite except for A1 and A2 that has a higher pearlite phase which is responsible for their high hardnesses [40].

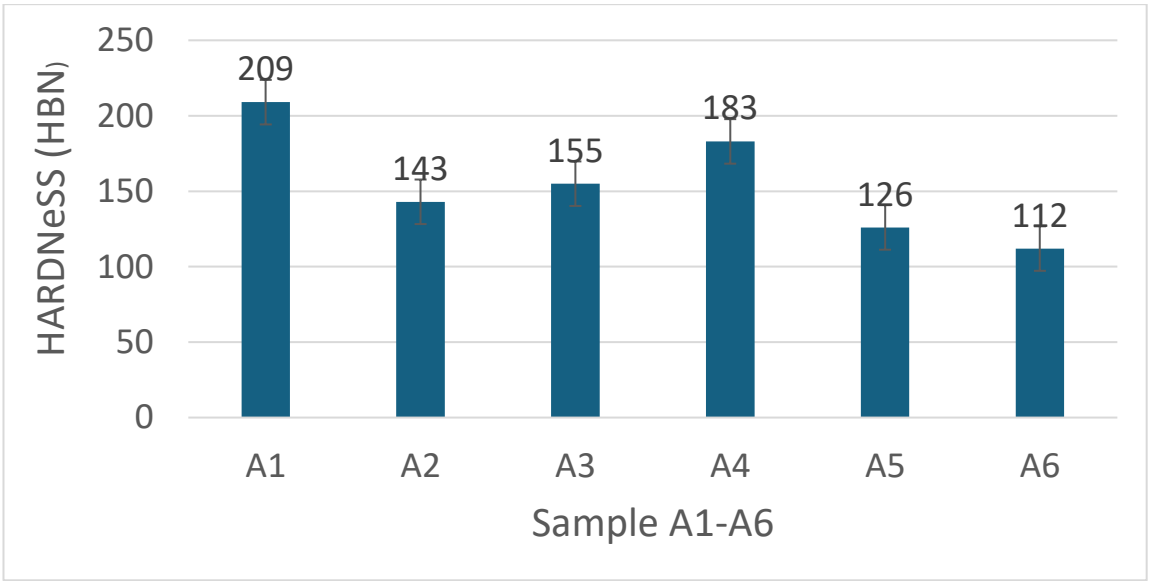

Fig. 7. Variation of Hardness heat-treated samples A1-A6

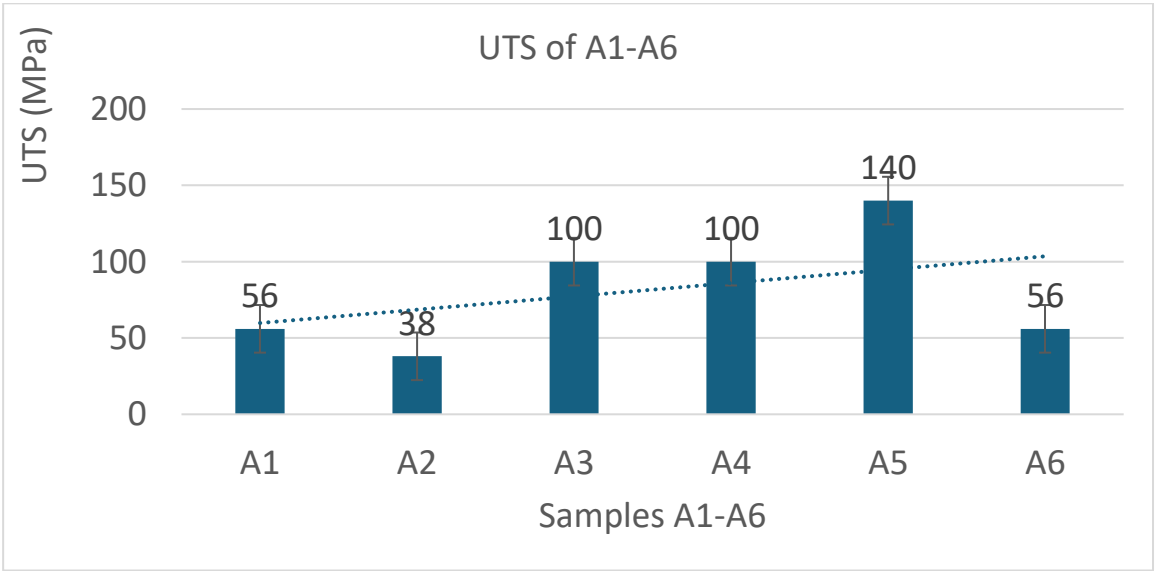

Fig. 8. Variation of UTS for Samples A1-A6

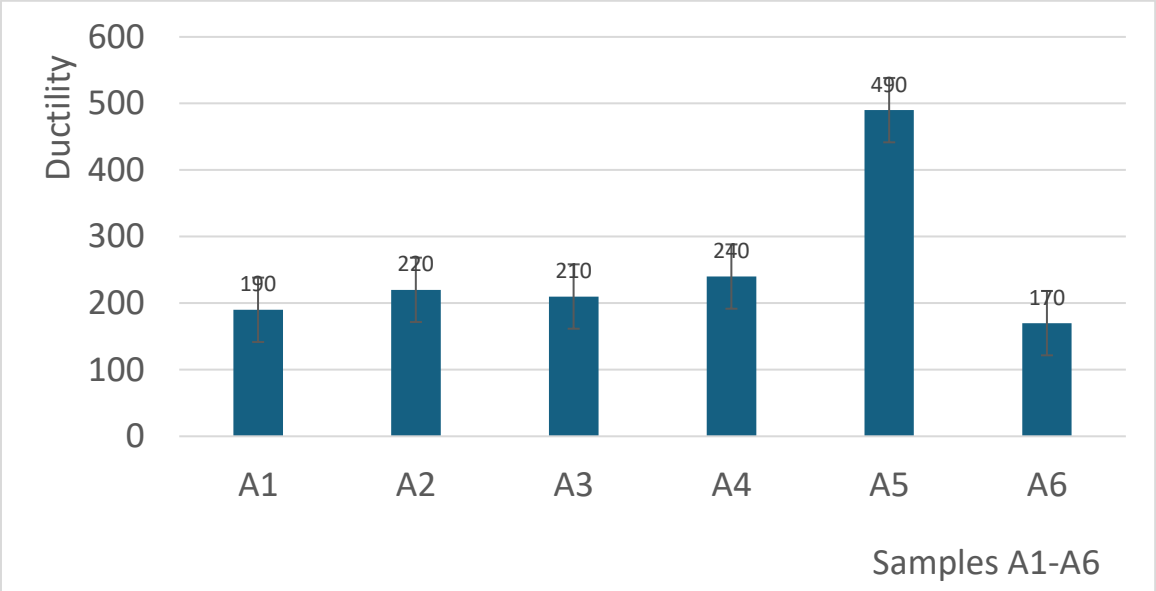

Fig. 9. Variation of Ductility with Samples A1-A6

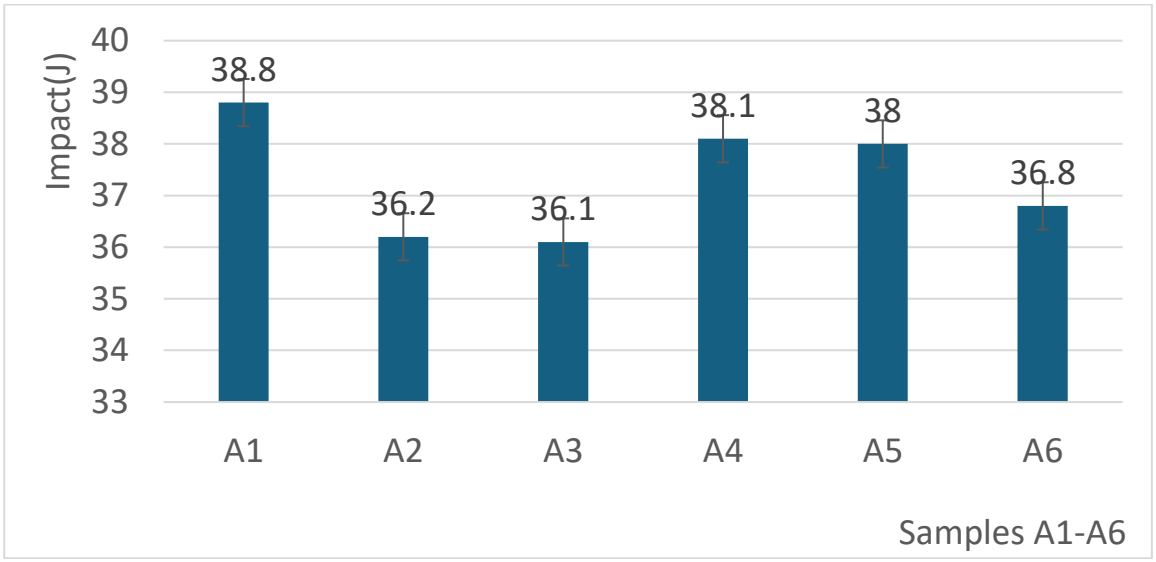

Fig. 10. Variation of Impact test with Samples A1-A6

3.3.2 Tensile test

The tensile test results for the CGI- heat-treated samples A1-A6 are shown in Fig. 8. The following was deducted from the graph. A5 has the highest ultimate tensile strength (UTS) value of 140 megapascals (MPa) and A2 has the lowest UTS value of 38 MPa. A1 and A6 have UTS values of 58 MPa, and A3 and A4 have 100MPa, respectively. The highest UTS of 140 MPa for A5 in the series is in agreement with [41]. That states that the UTS value of ductile iron is higher than that of gray cast iron due to alloying elements like magnesium, aluminum, and chromium additions. These elements promote ferritic microstructure over pearlite, and this is responsible for the H5 value.

3.3.3 Ductility

From Fig. 9 it can be deduced that A5 has the highest ductility of 490 due to the presence of magnesium as an alloying element that aids the transformations of α-ferritic microstructure over the pearlite phase which is in line with [42] and it is expected that ductile cast iron should have elasticity close to that of steel according to [43].

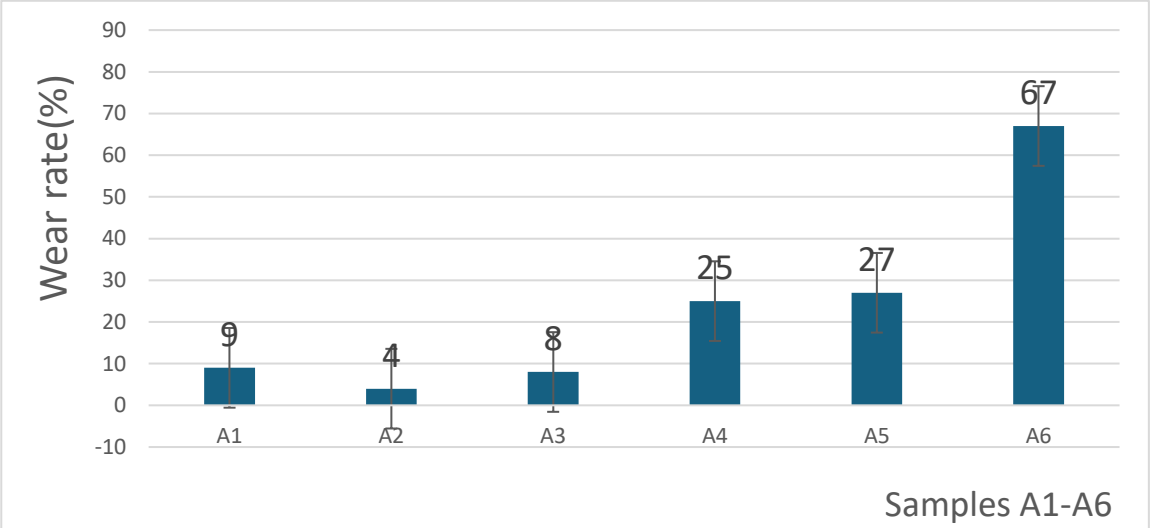

Fig. 11. Variation of Wear Rate of Samples A1-A6

3.3.4 Impact strength

Fig. 10, shows that A1 has the highest impact energy of 38.76 J/mm^2 in the series. This is normal because of surface hardening and the presence of copper and silicon in line with [44]. However, the differences in the impact energy are not much from A1 to A6. It can be seen clearly that the differences in A3, A4, and A6 are not that much because of the little variance in the pearlitic and ferritic phases. These sets of series are ideal and suitable for exhaust system outer body parts production according to [44,45].

3.3.5 Wear

Fig. 11 reveals, that A6 has the highest material loss with wear resistance of 66% for the series. The least material loss was A2 and A3 because they are gray cast iron with copper addition and because the pearlite microstructure phase is more predominantly present than the ferritic phase which conforms with [46].

4. CONCLUSION

The carbon equivalent of the fully annealed samples A1 to A6 was calculated, indicating that they are hypereutectic cast graphite irons.

Results from the SEM analysis indicated that A1 and A2 have a microstructure close to that of gray cast irons because of higher percentages of distorted graphite flakes (DGF), and A3 and A4 were compacted graphite cast iron (CGI), and A5 and A6 have structure close to ductile cast irons.

The mechanical properties of A1-A6 follow the thread of properties of gray, CGI, and ductile cast iron respectively in that order except where alloying elements and microstructure were employed to change the property. The hardness value of A4 and A3 a CGI, was higher than that of A2 a gray iron because of the addition of higher concentrations of copper, titanium, and manganese that promote pearlite structure. The presence of cementite in pearlitic cast irons leads to an increase in hardness.

Also, the thread follows in the UTS and ductility results except for A6 which has its values close to the A1 due to high percentages of aluminum, silicon, and chromium as an alloying element that promotes the ferrite phase. A CGI with a higher concentration of ferritic phase is usually ductile and ductility leads to higher tensile strength because the CGI matrix contains more nodular graphites.

In addition, the impact energy of gray cast iron was expected to be higher than that of CGI and ductile cast iron. A1 with 38.8J has the highest impact energy in the samples because it has its microstructure close to gray irons and A3 has the least impact energy with 36.1J because it alloying element promotes ferrite phases. Lastly, the wear rates of 67% and 27% of A6 and A5 were the highest in the series because they are ductile cast iron.

DISCLAIMER (ARTIFICIAL INTELLIGENCE)

Author(s) hereby declares that NO generative AI technologies such as Large Language Models

(ChatGPT, COPILOT, etc.) and text-to-image generators have been used during the writing or editing of this manuscript.

ACKNOWLEDGEMENTS

The research is supported by Petroleum Trust Development Funds (PTDF).

COMPETING INTERESTS

Authors have declared that no competing interests exist.

REFERENCES

1. Sergeant GF, Evans ER. Production and properties of compacted Graphite Irons. Br Foundrym. 2020;71(5):115–124.
2. Seidu SO, Oloruntoba DT, Otunniyi IO. Effect of shakeout time on microstructure and hardness properties of grey Cast Iron. J. Miner. Mater. Charact. Eng. 2014;02(04):346–350.
3. Seidu SO, Onigbajumo A. Graphitization behavior and mechanical property prediction model for grey cast Iron with Varying Wall Thickness Graphitization Behavior and Mechanical Property Prediction Model for Grey Cast Iron with Varying Wall Thickness; 2018.
4. Azeem MA, Bjerre MK, Atwood RC, Tiedje N, Lee PD., Synchrotron quantification of graphite nodule evolution during the solidification of cast Iron. Acta Mater. 2018;155:393–401.
5. Mohammed WM, Ng E, Elbestawi MA. Modeling the effect of the microstructure of compacted graphite iron on chip formation. Int. J. Mach. Tools Manuf; 2011.
6. Holmgren D, Källbom R, Svensson IL. Influences of the graphite growth direction on the thermal conductivity of cast Iron. Metall. Mater. Trans. A Phys. Metall. Mater. Sci; 2007.
7. Dawson S, Schroeder T. Practical applications for compacted graphite Iron. AFS Trans. 2004;34:698.
8. Essam MA, Shash AY, Megahed H, El-Kashif E. Effect of section thickness on microstructure and mechanical properties of compacted graphite Iron for diesel engine applications. Heliyon. 2021;7(1):e05930.
9. Ceschini L, Morri A, Morri A. Effects of casting size on microstructure and mechanical properties of spheroidal and compacted graphite Cast Irons: Experimental Results and Comparison with International Standards. J. Mater. Eng. Perform. 2017;26(6):2583–2592.
10. Bin Lin M, Wang CJ, Volinsky AA. High temperature oxidation behavior of flake and spheroidal graphite cast Irons. Oxid. Met. 2011;76(3–4):161–168.
11. Dawson S. Compacted graphite Iron: New opportunities for engine design. In SAE Technical Papers; 1995.
12. Paknikar PSK. The production technology of a modern material for heavy automotive vehicles - A Compacted Graphite Iron (C.G.I.). IRA-International J. Technol. Eng. (ISSN 2455-4480). 2016;3(2).
13. Aranke O, Algenaid W, Awe S, Joshi S. Coatings for automotive gray cast Iron brake discs: A review. Coatings. 2019;9(9).
14. Cole GS. Light weighting the automotive industry the road to 2025 café. In IMPC 2016 - 28th International Mineral Processing Congress. 2016;2016.
15. Behera A, Mishra SC. A novel material used in automotive industry: Compacted graphite Iron, Emerg. Mater. Res. 2012;1(5):271–274.
16. Ning H, et al. Effect of Ni and Mo on microstructure and mechanical properties of grey cast Iron. Mater. Technol., vol. 38, no. 1, 2023.
17. Sharma A, Goel SK. Materials science and engineering a effect of heat treatment on microstructure, mechanical properties and erosion resistance of cast 23-8-N nitronic steel. Mater. Sci. Eng. A. 2015;637: 56–62.
18. Oladele I, Alonge D, Betiku T, Barnabas A, Shittu S. Distinctiveness of welding joints design based on mechanical and corrosion environmental influence on low carbon steel. Adv. Technol. Mater. 2019;44(2):13–19.
19. Marques ESV, Silva FJG, Paiva OC, Pereira AB. Improving the mechanical strength of ductile cast Iron welded joints using different heat treatments. Materials (Basel). 2019;12(14).
20. Kim S, Cockcroft SL, Omran AM, Hwang H. Mechanical, wear and heat exposure properties of compacted graphite cast iron at elevated temperatures. J. Alloys Compd. 2009;487(1–2).
21. Fragassa C, Radovic N, Pavlovic A, Minak G. Tribology in industry comparison of mechanical properties in compacted and

spheroidal graphite Irons. 2016;38(1):45–56.
22. Lyu Y. Abrasive wear of compacted graphite cast Iron with Added Tin. Metallogr. Microstruct. Anal. 2019;8(1):67–71.
23. Yao M, Wang D, Zhao M. Element analysis based on energy-dispersive X-Ray Fluorescence. Adv. Mater. Sci. Eng. 2015;2015(1):1–7.
24. Rydberg J. Wavelength dispersive X-ray fluorescence spectroscopy as a fast, non-destructive and cost-effective analytical method for determining the geochemical composition of small loose-powder sediment samples. J. Paleolimnol. 2014;52(3):265–276.
25. Folorunso D, Bello S. Enhancement of the Mechanical and Thermal Integrity of Ijapo Clay for Thermal Insulation. J. Environ. Technol. 2021;2(1):30–38.
26. Gregorutti RW, Grau JE. Mechanical properties of compacted graphite cast Iron with different microstructures. Int. J. Cast Met. Res. 2014;27(5):275–281.
27. Enders MSP, et al. Characterization of inorganic solids present in Brazilian crude oil emulsions Using Scanning Electron Microscopy (SEM) with Energy-Dispersive X-ray Spectrometry (EDS): Evaluation of the Effect of Solvents. Energy and Fuels. 2020;34(2):1309–1316.
28. Hetzner DW. Microindentation hardness testing of materials using ASTM E384. Microsc. Microanal. 2003;9(SUPPL. 2):708–709.
29. Theophilus C, Addah NOCGL, Uzoma OC. Measuring the correlation between the tensile strength and hardness of steel and aluminum as alternative ship hull construction materials in Local Ship Yards in Nigeria. 2018;7:51–58.
30. Layton BE. A comparison of energy densities of prevalent energy sources in units of joules per cubic meter. Int. J. Green Energy. 2008;5(6):438–455.
31. Dongo EI, Seidu SO, Ogbodo FJ. No title the influence of indigenously sourced carbonaceous materials on the mechanical properties of Mild Steel for Industrial Application. Novel Perspectives of Engineering Research. 2022;9.
32. Boulifa MI, Hadji A. Study of the influence of alloying elements on the mechanical characteristics and wear behavior of a ductile cast Iron. Frat. ed Integrita Strutt. 2021;15(56):74–83.
33. Efremenko VG, Shimizu K, Cheiliakh AP, Kozarevskaya TV, Kusumoto K, Yamamoto K. Effect of vanadium and chromium on the microstructural features of V-Cr-Mn-Ni spheroidal carbide cast Irons. Int. J. Miner. Metall. Mater. 2014;21(11):1096–1108.
34. Medyński D, Janus A. Effect of heat treatment parameters on abrasive wear and corrosion resistance of austenitic nodular cast Iron Ni-Mn-Cu. Arch. Civ. Mech. Eng. 2018;18(2):515–521.
35. Biswas S, Monroe C, Prucha T. Use of published experimental results to validate approaches to gray and ductile Iron mechanical properties prediction. Int. J. Met. 2017;11(4):656–674.
36. Baer W. Chunky graphite in Ferritic spheroidal graphite cast Iron: Formation, prevention, characterization, impact on properties: An Overview. Int. J. Met. 2020;14(2):454–488.
37. Elena Garcia Trelles Stefan Eckmann Christoph Schweizer. Experimental characterization of the short crack growth behavior of a ductile cast Iron (DCI GJS-500) affected by intergranular embrittlement at temperatures nearby 400. No TitleInternational J. Fatigue. 2020;155(106573).
38. Panov AG, Gurtovoy DA, Shaekhova IF. About the possibility of increase in CGI properties by austempering. Solid State Phenom. 2018;284 SSP:224–228.
39. Aghareb Parast MS, Jamalkhani Khameneh M, Azadi M, Azadi M, Mahdipanah MH, Roostaie S. Effect of plasma nitriding on high-cycle fatigue properties and fracture behaviors of GJS700 nodular cast Iron under cyclic bending loading. 2021;44(8):2070–2086.
40. García LN, Tolley AJ, Carazo FD, Boeri RE. Identification of Cu-rich precipitates in Pearlitic spheroidal graphite cast Irons. Mater. Sci. Technol. (United Kingdom). 2019;35(18):2252–2258.
41. Sckudlarek W, Krmasha MN, Al-Rubaie KS, Preti O, Milan JCG, Da Costa CE. Effect of austempering temperature on microstructure and mechanical properties of ductile cast Iron modified by niobium. J. Mater. Res. Technol. 2021;12:2414–2425.
42. Bellini C, Di Cocco V, Favaro G, Iacoviello F, Sorrentino L. Ductile cast Irons: Microstructure influence on the fatigue initiation mechanisms. Fatigue Fract. Eng. Mater. Struct. 2019;42(9):2172–2182.

43. Ikeda T, Noda NA, Sano Y. Conditions for notch strength to be higher than static tensile strength in high–strength ductile cast Iron. Eng. Fract. Mech. 2019;206(2018):75–88.
44. Górny M, Angella G, Tyrała E, Kawalec M, Paź S, Kmita A. Role of Austenitization temperature on structure homogeneity and transformation kinetics in austempered Ductile Iron. Met. Mater. Int. 2019;25(4):956–965.
45. Kucharska B, Moraczyński O. Exhaust system piping made by hydroforming: Relations between stresses, microstructure, mechanical properties and surface. Arch. Civ. Mech. Eng. 2020;20(4):1–11.
46. Gonzaga RA. Influence of ferrite and pearlite content on mechanical properties of ductile cast Irons. Mater. Sci. Eng. A. 2013;567:1–8.

Peer-review history:
The peer review history for this paper can be accessed here:
https://www.sdiarticle5.com/review-history/124216